Chinese Journal of Natural Medicines

(+)-Strebloside induces Non-Hodgkin lymphoma cell death through the STEAP3-Mediated Ferroptosis and MAPK pathway

Yu Zhao, Jing Cai, Ying Yang, Dongmei Zhang, Jiayi Ren, Shuyun Xiao, Jian Xu, Feng Feng, Rong Wu, Jie Zhang

Citation: Yu Zhao, Jing Cai, Ying Yang, Dongmei Zhang, Jiayi Ren, Shuyun Xiao, Jian Xu, Feng Feng, Rong Wu, Jie Zhang, (+)-Strebloside induces Non-Hodgkin lymphoma cell death through the STEAP3-Mediated Ferroptosis and MAPK pathway, Chinese Journal of Natural Medicines, 2025, 23(10), 1221-1231. doi: 10.1016/S1875-5364(25)60873-9.

View online: https://doi.org/10.1016/S1875-5364(25)60873-9

Chinese Journal of Natural Medicines 23 (2025) 1221-1231

Contents lists available at ScienceDirect

Chinese Journal of Natural Medicines

journal homepage: www.cjnmcpu.com/

Original article

(+)-Strebloside induces Non-Hodgkin lymphoma cell death through the STEAP3-Mediated Ferroptosis and MAPK pathway

Yu Zhao[a,Δ], Jing Cai[a,Δ], Ying Yang[a], Dongmei Zhang[a], Jiayi Ren[a], Shuyun Xiao[a], Jian Xu[a], Feng Feng[a,b], Rong Wu[c,*], Jie Zhang[a,*]

[a] *School of Traditional Chinese Pharmacy, China Pharmaceutical University, Nanjing 210009, China*
[b] *School of Pharmacy, Nanjing Medical University, Nanjing 211198, China*
[c] *Chongqing Wanzhou Food and Drug Inspection Institute, Chongqing Key Laboratory of Development and Utilization of Genuine Medicinal Materials in the Three Gorges Reservoir Area, Chongqing 404100, China*

ARTICLE INFO

Article history:
Received 23 September 2024
Revised 6 November 2024
Accepted 13 November 2024
Available online 20 October 2025

Keywords:
Non-Hodgkin lymphoma
(+)-Strebloside
Antitumor activity
MAPK
Ferroptosis

ABSTRACT

(+)-Strebloside, a significant bioactive compound isolated from the roots of *Streblus asper* Lour., demonstrates inhibitory effects against multiple malignancies. However, its specific function and underlying mechanistic pathways in Non-Hodgkin lymphoma (NHL) remain unexplored. This investigation sought to elucidate the role and potential mechanisms of (+)-strebloside-induced NHL cell death. The results demonstrated that (+)-strebloside significantly induced apoptosis and ferroptosis in NHL cells, including those from Raji cell-derived xenograft models. Mechanistic analyses revealed that (+)-strebloside enhanced six-transmembrane epithelial antigen of prostate 3 (STEAP3)-induced ferroptosis in NHL, and STEAP3 inhibition reduced the proliferation-inhibitory effects of (+)-strebloside. Furthermore, (+)-strebloside suppressed NHL proliferation through the mitogen-activated protein kinase (MAPK) pathway, and extracellular signal-regulated kinase (ERK) inhibition diminished the proliferation-inhibitory activity induced by (+)-strebloside. These findings indicate that (+)-strebloside presents promising therapeutic potential for NHL treatment.

1. Introductions

Non-Hodgkin lymphoma (NHL) represents the predominant subtype within the lymphoma classification, comprising approximately 90% of all lymphoma cases [1]. It is the sixth most prevalent malignancy [2], presenting a substantial public health challenge. Currently, R-CHOP-based chemotherapy protocols remain the most effective treatment modalities for NHL [3–5]. However, intensive chemotherapy can result in myelosuppression and potentially fatal complications. Furthermore, tumor progression and chemotherapy may enhance coagulation risk, limiting therapeutic options for patients with thrombotic predisposition. Alternative clinical interventions for NHL include CAR-T cell therapy [6], bispecific antibody immunotherapy [7, 8], lenalidomide [9], and targeted therapies such as BTK and PI3K inhibitors [10]. Although these therapeutic strategies have enhanced survival and cure rates among NHL patients, their clinical application remains limited due to substantial costs and adverse effects [11–13]. Thus, identifying novel interventions and elucidating anti-tumor mechanisms remains crucial for expanding NHL treatment options.

Natural products (NPs) constitute a valuable source of anti-tumor-active compounds that provide diverse structural frameworks for discovering novel NHL therapeutic agents. The investigation of potential NPs may yield additional treatment options for NHL, establishing a foundation for developing or optimizing new anti-tumor medications. Cardiac glycosides (CGs) comprise a class of naturally occurring secondary metabolites recognized for their specific inhibitory effects on Na^+/K^+-ATPase (NKA) [14, 15]. (+)-Strebloside, isolated from the roots of *Streblus asper* Lour. [16], exhibits proliferation-inhibitory effects against various human and mammalian malignant cell types, including cervical cancer, ovarian cancer, non-small cell lung cancer, and melanoma cells. Mechanistic investigations have demonstrated that (+)-strebloside induces apoptosis by inhibiting NKA and NF-κB activation in ovarian cancer cells [17].

Despite extensive documentation of CGs' anti-cancer properties, research regarding their pharmacological mechanisms remains limited. These mechanisms potentially involve multiple signaling pathways, including the membrane pump NKA, Src-EGFR-Ras-Raf-mitogen-activated protein kinase (MAPK) signaling, and topoisomerase 2 [18]. Ferroptosis represents a regulated form of non-apoptotic cell death characterized by iron accumulation and lipid peroxide formation [19]. Cancer cells require elevated levels of iron and lipid metabolism for growth compared to normal cells, theoretically increasing their ferroptosis sensitivity [20]. Consequently, targeted ferroptosis presents a promising cancer treatment strategy. The six-transmembrane epithelial antigen of prostate 3 (STEAP3), a STEAP family member, participates in iron balance regulation [21]. Moreover, STEAP3 functions as a metal reductase, facilitating ferric ion (Fe^{3+}) to ferrous iron (Fe^{2+}) conversion within the body. Evidence increasingly suggests

* Corresponding author.
E-mail addresses: 185634082@qq.com (Rong Wu); 1020152495@cpu.edu.cn (Jie Zhang)
Δ These authors contributed equally to this work.

https://doi.org/10.1016/S1875-5364(25)60873-9

STEAP3's critical role in lysosomal iron metabolism and ferroptosis regulation [22, 23].

While (+)-strebloside demonstrates promising anti-tumor potential, its anti-non-Hodgkin lymphoma properties remain unexplored. This study investigated (+)-strebloside's anti-proliferative effects on NHL cells both *in vivo* and *in vitro*. The research evaluated (+)-strebloside's safety profile and general tumor prognostic indicators. Subsequently, specific mechanisms were examined. This investigation revealed, for the first time, that (+)-strebloside may exert anti-NHL effects through the STEAP3-mediated ferroptosis pathway and MAPK pathway.

2. Materials and methods

2.1. Cells, compound, and mice

Human Burkitt lymphoma cell line Raji was obtained from Shanghai Cell Bank of Chinese Academy of Sciences (Shanghai, China), authenticated by STR profiling. Human T lymphocyte cell line Jurkat and diffuse large B-cell lymphoma cell line OCI-LY3 were provided by Zhejiang University.

(+)-Strebloside (provided by the School of Traditional Chinese Medicine, China Pharmaceutical University, China) was dissolved in dimethyl sulfoxide (DMSO, Sigma Aldrich), stored at −20 °C, and diluted with medium and freshly prepared before each use.

Female BALB/c nude mice were obtained from Shanghai National Center for Laboratory Animals (Shanghai, China) and maintained in a pathogen-free environment. The mice received adequate food and water under controlled conditions: ambient relative humidity of 50%–60%, temperature of 22–26 °C, and a 12 h light/dark cycle. Euthanasia was performed *via* cervical dislocation. All animal experiments were conducted in accordance with institutional guidelines for animal care and use, with approval from the Pharmaceutical Animal Experiment Center of China Pharmaceutical University (No. 2021-12-002).

2.2. Cell culture

Raji, Jurkat, and OCI-LY3 cells were cultured in RPMI-1640 medium containing 10% fetal bovine serum (FBS; Gibco, USA). The cultures were maintained at 37 °C in an incubator with 5% CO_2.

2.3. Cell viability assay

Cells were seeded in 96-well plates at 1000 cells per well. Cell counting kit-8 (CCK-8; Beyotime, Shanghai, China) was added to each well and incubated for 2 to 4 hours at 37 °C. The optical density (OD) was measured at wavelengths of 450 nm and 650 nm using a microplate reader at specified intervals. Cell viability was calculated relative to the solvent (DMSO) control. The 50% inhibitory concentration (IC_{50}) was determined using GraphPad Prism 9.3.0 software.

2.4. Colony formation assay

Colony formation in soft agar was performed by seeding approximately 1×10^4 Raji and Jurkat cells in the upper layer (0.7% agarose) of a two-layer agar system (0.7% and 1.2%) in 6-well culture plates. After 3 weeks, colonies (defined as > 50 cells) were counted, and clonogenicity (%) was calculated as the number of colonies/total growing cell number × 100%.

2.5. Cell cycle and apoptosis analysis

Cells were seeded in 6-well plates, synchronized in serum-free medium for 24 h, and subsequently cultured in medium containing 10% FBS for the designated period.

Cell apoptosis rates were determined using flow cytometry with the Annexin V-fluorescein isothiocyanate (FITC) apoptosis detection kit (Key-GEN, Nanjing, China), following manufacturer's instructions. A 2 mL suspension containing 10^5 cells was treated with Annexin-V-FITC and propidium iodide (PI) kit solution and incubated in darkness for 15 minutes. Analysis was performed using FACS Calibur Flow Cytometry (BD, USA).

For cell cycle analysis, cells were analyzed through Flow cytometry using a cell cycle detection kit (Key-GEN, Nanjing, China). A 2 mL suspension containing 10^6 cells was fixed in 70% ethanol overnight, treated with RNase A for 30 min, and stained with PI. Analysis was conducted using FACS Calibur Flow Cytometry (BD, USA) at 488 nm.

2.6. Tumor growth in xenografts

In the cell-derived xenograft model, Raji cells (1×10^7 cells/100 μL) were injected subcutaneously into BALB/c nude mice. Tumor volumes were measured and calculated every two days using the formula $V = a^2b/2$, where "a" represents the smallest superficial diameter and "b" represents the largest superficial diameter. When tumors reached approximately 50 mm^3, mice were randomly assigned to groups and received intraperitoneal injections of doxorubicin, (+)-strebloside (2 or 4 $mg \cdot kg^{-1}$) or physiological saline every two days. Tumor development and overall health were monitored every two days. After 14 d of treatment, mice were euthanized, and tumors were excised and measured.

2.7. Acute toxicity test in mice

Four-week-old female BALB/c nude mice weighing 18–22 g were randomly divided into three equal groups: control (Sanitary saline, i.p.) and treatment groups (10 or 20 $mg \cdot kg^{-1}$, i.p.). Mice received a single dose of treatment. After 14 days, the mice were euthanized, and their heart, liver, spleen, lungs, kidneys, and lymph nodes were harvested.

2.8. Proteomic analysis

The quantitative proteomic analysis involved homogenizing control tumors and those treated with (+)-strebloside in a co-immunoprecipitation lysis buffer containing 8 $mmol \cdot L^{-1}$ urea and 1% protease inhibitor cocktail to prepare total protein samples. A total of 100 μg of protein from each sample underwent mass spectrometry analysis, with debris removed through centrifugation. For the initial overnight digestion, trypsin was added at a 1∶50 ratio (trypsin to protein mass). Each peptide channel was labeled with its respective TMT reagent (following the manufacturer's protocol, ThermoFisher Scientific) and incubated for 2 h at room temperature. The pooled samples were desalted with a Strata X C_{18} SPE column (Phenomenex) and dried by vacuum centrifugation. The tryptic peptides were dissolved in solvent A (0.1% formic acid and 2% acetonitrile in water), and directly loaded onto a homemade reversed-phase analytical column (25 cm length, 75 mm i.p.). Peptides were separated with a gradient from 6% to 24% solvent B (0.1% formic acid in 100% acetonitrile) over 60 min, 24% to 35% in 22 min, up to 80% in 4 min, and then maintained at 80% for 4 min, all at a constant flow rate of 450 $nL \cdot min^{-1}$ on an EASY-nLC 1200 UPLC system (ThermoFisher Scientific). The separated peptides were characterized by a Q Exactive HF-X mass spectrometer (Thermo-Fisher Scientific) with a nano-electrospray ion source. Gene Ontology (GO) annotation proteome was derived from the UniProt-GOA database (http://www.ebi.ac.uk/GOA/). Proteins were classified using GO annotations into three distinct groups: biological process, cellular com-

ponent, and molecular function. For functional enrichment analysis, proteins were categorized based on GO biological process annotations. A two-tailed Fisher's exact test was employed to assess the enrichment of the differentially expressed proteins compared to all identified proteins. The GO with *P*-values < 0.05 was considered significant.

2.9. Hematoxylin and eosin (H&E) staining and immunohistochemistry (IHC)

For H&E staining, the tumors and tissues were preserved in formaldehyde and subsequently embedded in paraffin. Sections measuring 5 mm in thickness were prepared for H&E staining following a standard procedure. Images were captured using a Pannoramic MIDI II.

To detect the expression of ki-67, p53, and STEAP3 in tumor samples, the sections underwent dehydration using increasing concentrations of ethanol, and endogenous peroxidase activity was inhibited with a 3% (*V*/*V*) hydrogen peroxide solution in methanol for 10 minutes. Antigen retrieval was performed using a 1 mM EDTA buffer (pH 9.0) in a microwave. The sections were then incubated with antibodies, developed using the Envision Detection System (Dako), and counterstained with hematoxylin. The antibodies utilized in this research are listed in Table S1.

2.10. Western blot analysis

Proteins were extracted from the cells, and their concentrations were determined using the BCA protein assay (Beyotime, Shanghai, China). Equal quantities of the proteins underwent analysis using 10% SDS polyacrylamide gel electrophoresis and were subsequently transferred to PVDF membranes (Merck Millipore, USA). The membranes were incubated for 2 hours at room temperature with 5% non-fat dry milk for blocking, followed by treatment with diluted primary antibodies overnight at 4 °C. The membranes were then incubated with horseradish peroxidase-conjugated goat anti-rabbit or mouse secondary antibody (Beyotime, Shanghai, China) for 2 h at room temperature. Tubulin-α and *β*-actin (Beyotime, Shanghai, China) served as the internal control. Chemiluminescence (Tanon, Shanghai, China) was employed to visualize the signals, and ImageJ software was utilized for image analysis. The antibodies utilized in this research are listed in Table S1.

2.11. Ribonucleic acid (RNA) extraction and reverse transcription quantitative polymerase chain reaction (RT-qPCR) assay

Cells were processed to extract total RNA using the Total RNA Extraction Kit (YiFeiXue Biotechnology, Nanjing, China). Real-time PCR was performed using 2 × SYBR Green Fast qPCR Master Mix (YiFeiXue biotechnology, Nanjing, China) according to the manufacturer's instructions on a BIO-RAD S1000 device (BIO-RAD) S1000 device (BIO-RAD, USA). RT of total RNA and cDNA synthesis were analyzed separately using different procedures. The mRNA level was normalized to the expression of *β*-actin and calculated *via* the standard $2^{-\Delta\Delta Ct}$ method. All primers used in this study are listed in Table S2 and were synthesized by Servicebio (Wuhan, China).

2.12. Ferrous ion detection

For intracellular ferrous ion detection, the 5 μmol·L^{-1} FeRhoNox-1 fluorescent probe (Maokang Biotech, Shanghai, China) was incubated with cells and analyzed using flow cytometry at 532 nm excitation wavelength.

2.13. Reactive oxygen species (ROS) and lipid peroxidation assay

Lipid peroxidation levels were measured using BODIPY-C11 dye (MCE). Cells were seeded in a 6-well plate and cultured overnight. Subsequently, cells were collected and resuspended in fresh medium containing 5 μmol·L^{-1} BODIPY-C11, incubated at 37 °C for 20 min, washed twice with phosphate-buffered saline (PBS), and analyzed by flow cytometry.

The detection of ROS was performed using a ROS assay kit (Beyotime, Shanghai, China). Cells were suspended in blank culture medium containing 10 μmol·L^{-1} dichloro-dihydro-fluorescein diacetate (DCFH-DA). Following incubation at 37 °C for 30 min, cells were washed twice with PBS and analyzed using flow cytometry.

2.14. Mitochondrial membrane potential (ΔΨm)

For intracellular mitochondrial membrane potential (ΔΨm) assay, cells were gently resuspended in pre-warmed Mito-Tracker Red CMXRos working solution (Beyotime, Nanjing, China) at 37 °C and incubated for 15–30 min. After incubation, cells were washed with PBS and analyzed using FACS Calibur flow cytometry (BD, USA) at 579 nm.

2.15. Adenosine 5′-triphosphate (ATP) production

ATP levels in cells were determined using the ATP assay kit (Beyotime, Nanjing, China). Cells were collected and lysed thoroughly with Vortex lysis solution, and the supernatant was collected. ATP concentration was measured using SpectraMax® L (luminometer) and calculated against a standard curve prepared with ATP standard solution.

2.16. Cell transfection

Small interfering RNA (siRNA) was obtained from Sangon Biotech, and transfection reagents were supplied by Genepharma. Detailed sequences are provided in the supplementary material. Briefly, small RNA was diluted in buffer, combined with transfection reagents, and added to the cells. The target sequence of si-STEAP3 was UUGUAGGCAUAGAAGCAGACGTT.

2.17. Statistical analysis

Statistical analysis was performed using Excel and GraphPad Prism 9.3.0. Results are expressed as mean ± SD from three independent experiments, unless otherwise specified. Statistical significance between two groups was determined using a two-tailed, unpaired Student's *t*-test, with *P*-values below 0.05 considered statistically significant.

3. Results

3.1. (+)-Strebloside inhibits NHL proliferation activity and causes G_2/M arrest in vitro

The inhibitory effect of (+)-strebloside (Fig. 1A) on cell proliferation was evaluated using the CCK-8 assay in various NHL cell lines, including Raji, Jurkat, and OCI-LY3. Results demonstrated that NHL cell survival decreased in a concentration-dependent manner following (+)-strebloside treatment. In Raji cells, the IC_{50} values for (+)-strebloside treatment at 24, 48, and 72 h were 0.436, 0.278, and 0.098 μmol·L^{-1}, respectively (Fig. 1B). Additionally, both Jurkat and OCI-LY3 cell lines exhibited similar growth inhibition patterns in a concentration-dependent manner when treated with varying concentrations of (+)-strebloside for 24 hours, with IC_{50} values of 0.317 and 0.186 μmol·L^{-1}, respectively (Fig. 1C). In soft agar plate cloning experiments, Raji and Jurkat cells demonstrated reduced clone formation compared to con-

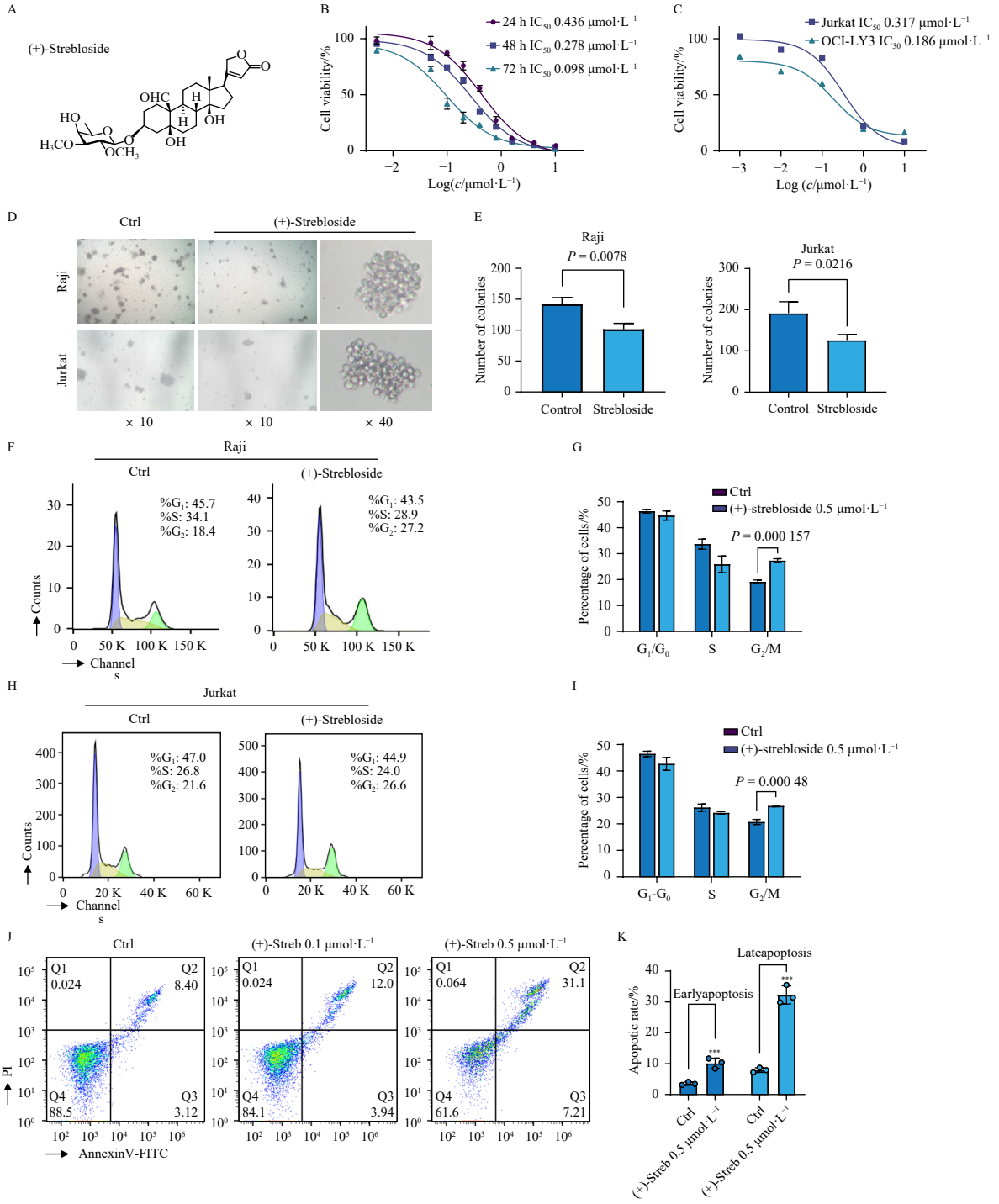

Fig. 1 (+)-Strebloside inhibits cancer cell proliferation and causes G_2/M arrest in NHL. (A) The structure of (+)-strebloside. (B–C) The viability of Raji, Jurkat, and OCI-LY3 cells at different concentrations and incubation times of (+)-strebloside were determined by CCK-8 assay (n = 3). (D) Proliferation inhibitory ability of (+)-strebloside on NHL cell lines was assessed by soft agar plate cloning assay(n = 3). (E) Quantitative statistical plots of soft agar plate cloning. (F–I) Cell cycle alterations in Raji and Jurkat cells after treatment with (+)-strebloside at a concentration of 0.5 μmol·L^{-1} for 24 h, and the quantitative statistical plots of cell proportions at different periods (n = 3). (J) Apoptotic cell populations after 24 h treatment with different concentrations of (+)-strebloside (n = 3). (K) Quantitative statistics of the proportion of early apoptotic and late apoptotic cells in control and (+)-strebloside treated groups. Results are expressed as mean ± SD. $^{*}P < 0.05$; $^{**}P < 0.01$; $^{***}P < 0.001$; ns, not significant. (+)-streb, (+)-strebloside.

trols when treated with non-lethal concentrations of (+)-strebloside ($P < 0.05$, Figs. 1D and 1E).

The influence of (+)-strebloside on the NHL cell cycle was investigated through PI staining. Following incubation of Raji and Jurkat cells with (+)-strebloside for 24 h, the proportion of cells in the G_2/M phase increased, indicating cell division arrest and demonstrating that (+)-strebloside exhibited a significant effect on the cell cycle of the lymphoma cell lines (Figs. 1F–1I).

Furthermore, Annexin V-FITC/PI staining demonstrated that (+)-strebloside induced apoptosis in Raji cells, with the percentage of apoptotic cells increasing in a dose-dependent manner (Fig. 1J). In comparison to the control group, treatment with 0.5 μmol·L^{-1} (+)-strebloside produced a significant difference in the percentage of both early and late apoptotic cells ($P < 0.001$, Fig. 1K).

3.2. (+)-Strebloside impedes the growth and metastasis of NHL in vivo

Tumor xenografts established with the Raji cell line were em-

ployed to assess the anti-tumor efficacy of (+)-strebloside in BALB/c nude mice. The mice received intraperitoneal injections of 4 mg·kg^{-1} as a high dose and 2 mg·kg^{-1} as a low dose of (+)-strebloside, with doxorubicin serving as a positive control and saline as a control. Following 2 weeks of drug treatments (Fig. 2A), tumors subcutaneously transplanted in nude mice were harvested and photographed (Fig. 2B).

In the excised subcutaneous transplanted tumors, the average tumor weight of 0.391 ± 0.138 g in the control group significantly exceeded that of 0.105 ± 0.096 g and 0.073 ± 0.054 g in the (+)-strebloside low-dose and high-dose treated groups ($P < 0.01$, Fig. 2C). Additionally, the average tumor volume observed in the control group was 631.17 ± 317.16 mm^3. In comparison, the average tumor volumes in the low-dose and high-dose (+)-strebloside treatment groups were 281.29 ± 120.34 and 183.80 ± 80.03 mm^3, respectively (Fig. 2D), showing a significant reduction relative to the control group. These results indicate that (+)-strebloside effectively inhibited tumor growth in nude mice with > 75% tumor inhibition (Fig. S1). The body weight of nude mice was monitored throughout the drug treatment process to assess general health and drug toxicity. Statistical analysis revealed no significant differences in body weight among the groups before and after the treatment (Fig. 2E).

An immunohistochemical analysis of excised mouse tumors was conducted *in vivo* to investigate the potential role of (+)-strebloside. The analysis revealed that (+)-strebloside reduced the expression of ki-67 and p53 (Figs. 2F and 2G), indicating a potential improvement in prognosis [24, 25]. H&E staining of axillary lymph nodes demonstrated that while the control group exhibited lymph node involvement and multiple metastases, mice treated with 4 mg·kg^{-1} of (+)-strebloside showed minimal axillary lymph node involvement (Fig. 2H), indicating that (+)-strebloside treatment inhibited tumor progression. Furthermore, terminal deoxynucleotidyl transferase-mediated dUTP nick end labeling (TUNEL) staining results demonstrated significantly higher apoptosis rates in tumor tissues from mice in the high-dose (+)-strebloside treatment group compared to the control group (Figs. 2F and 2I).

Safety assessments were also performed through acute toxicity tests of (+)-strebloside in mice. Following administration of a single dose of (+)-strebloside (10/20 mg·kg^{-1}), mice exhibited normal behavior patterns. The mice maintained stable weight over the two-week observation period (Fig. S1). After euthanization on day 14, examination of the heart, liver, spleen, lungs, kidneys, and lymphatic tissues revealed no visible lesions. H&E staining analysis of tissue morphology indicated no significant toxic effects (Fig. S1).

3.3. Proteomics reveals (+)-strebloside-mediated dysregulation of ionic homeostasis and oxidative stress in NHL

To elucidate the mechanisms of (+)-strebloside's effects on

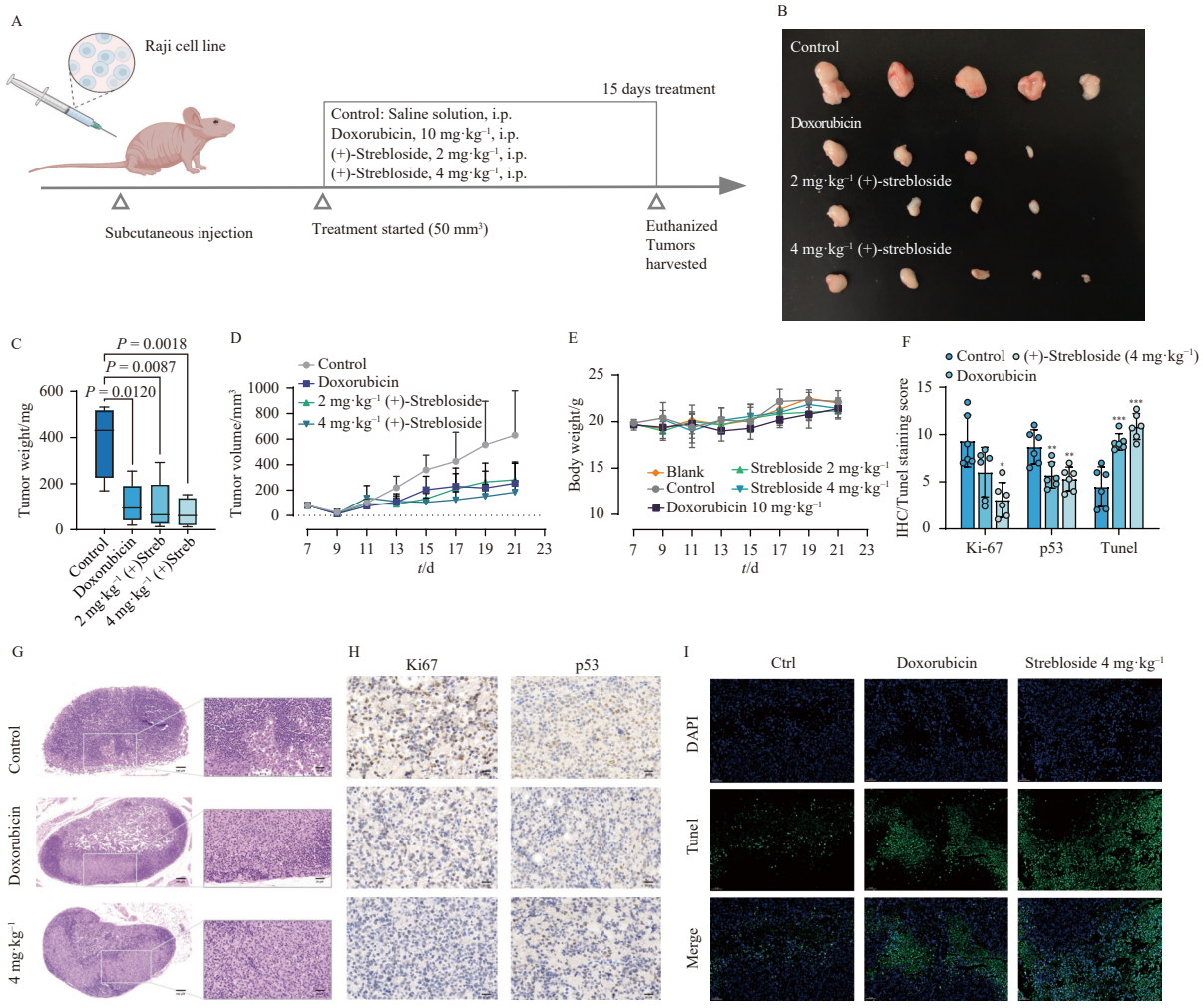

Fig. 2 (+)-Strebloside inhibited the NHL growth *in vivo*. (A) Flow chart for subcutaneous tumorigenesis model and drug treatment in nude mice. (B) The images of the exfoliated tumors ($n = 5$). (C, D) The volume and weight of the tumors in the subcutaneous tumorigenesis model ($n = 5$). (E) The body weight of tumor-bearing mice ($n = 5$). (F) Schematic representation of quantitative Ki-67 and p53 immunohistochemical staining, and TUNEL staining scores ($n = 6$). (G) Ki-67 and p53 immunohistochemical staining of subcutaneous transplanted tumor tissues in mice. (H) H&E staining of mouse lymphoid tissues. (I) TUNEL staining of subcutaneous transplanted tumor tissues in mice. Results are expressed as mean ± SD. $^{*}P < 0.05$; $^{**}P < 0.01$; $^{***}P < 0.001$. (+)-Streb, (+)-Strebloside.

NHL, proteomic analysis was performed on tumors from mice treated with 4 mg·kg^{-1} of (+)-strebloside and control groups (Fig. 3A). The analysis identified 52 up-regulated and 10 down-regulated proteins (ploidy change > 1.5). Enrichment analysis of biological processes revealed 43 proteins associated with lipid peroxidation and inorganic ion binding processes based on GO annotations ($P < 0.05$) (Table S3). Functional enrichment analysis showed significantly elevated levels of eight oxidative stress-related proteins in the high-dose (+)-strebloside group (Fig. 3B), alongside increased cytochrome c activity and enhanced fatty acid metabolism. The majority of differential proteins were localized to mitochondria (29.03%) (Fig. 3C), including several respiratory chain complex components. As primary sites of ROS generation, compromised mitochondrial function can lead to increased ROS production, potentially causing oxidative stress and cellular damage. The analysis revealed decreased calcium binding, metal ion binding, and cation binding activities, along with reduced intracellular calcium and metal ion homeostasis (Fig. 3B). This suggests that (+)-strebloside, a CG acting as a natural NKA ligand, may inhibit ion pumps and disrupt intracellular ion homeostasis. Additionally, proteomics identified increased STEAP3 protein expression (1.664) and 11 other iron ion transport-related proteins (Table S4), suggesting iron ions' potential role in (+)-strebloside-induced NHL cell death.

3.4. (+)-Strebloside upregulates STEAP3 protein and mediates ferrous iron overload

IHC staining demonstrated significantly elevated STEAP3 expression in tumor sections from (+)-strebloside-treated mice compared to the control group (Fig. 4A). Similar results were confirmed in Raji cells through Western blot and qPCR analyses (Figs. 4B–4D).

STEAP3, a metal-reducing enzyme, catalyzes the conversion of Fe^{3+} to Fe^{2+} within biological systems. The levels of ferrous ions inside the cells were evaluated using a fluorescent probe for ferrous ions (FerroFarRed). As demonstrated in Figs. 4E and 4F, the intracellular ferrous ion concentration increased after (+)-strebloside treatment in Raji and Jurkat cells, indicating that elevated STEAP3 levels enhanced ferrous ion accumulation in NHL cells.

3.5. Deferasirox or ferrostatin-1 (Fer-1) alleviates (+)-strebloside mediated enrichment of ferrous ions and inhibition of NHL proliferation

Deferasirox, an iron-selective binding agent, decreased intracellular ferrous ion levels in Raji cells when administered with (+)-strebloside, and enhanced cell viability during chelation compared to control cells ($P < 0.05$, Figs. 4G–4I). These results indicate that iron chelation decreased iron ion production and attenuated the growth suppression induced by (+)-strebloside.

The ferroptosis inhibitor Fer-1 similarly reduced the elevated intracellular ferrous ions induced by (+)-strebloside (Figs. 4J and 4K), protecting Raji cells from (+)-strebloside-mediated proliferation inhibition (Fig. 4L). These observations suggest that an iron-dependent programmed cell death pathway may contribute to (+)-strebloside toxicity.

These findings suggest that (+)-strebloside induces ferroptosis in NHL cells through modulation of the iron metabolic pathway [26]. Fe^{3+} undergoes STEAP3-mediated transformation to Fe^{2+} intracellularly before cytoplasmic release. Excessive Fe^{2+} accumu-

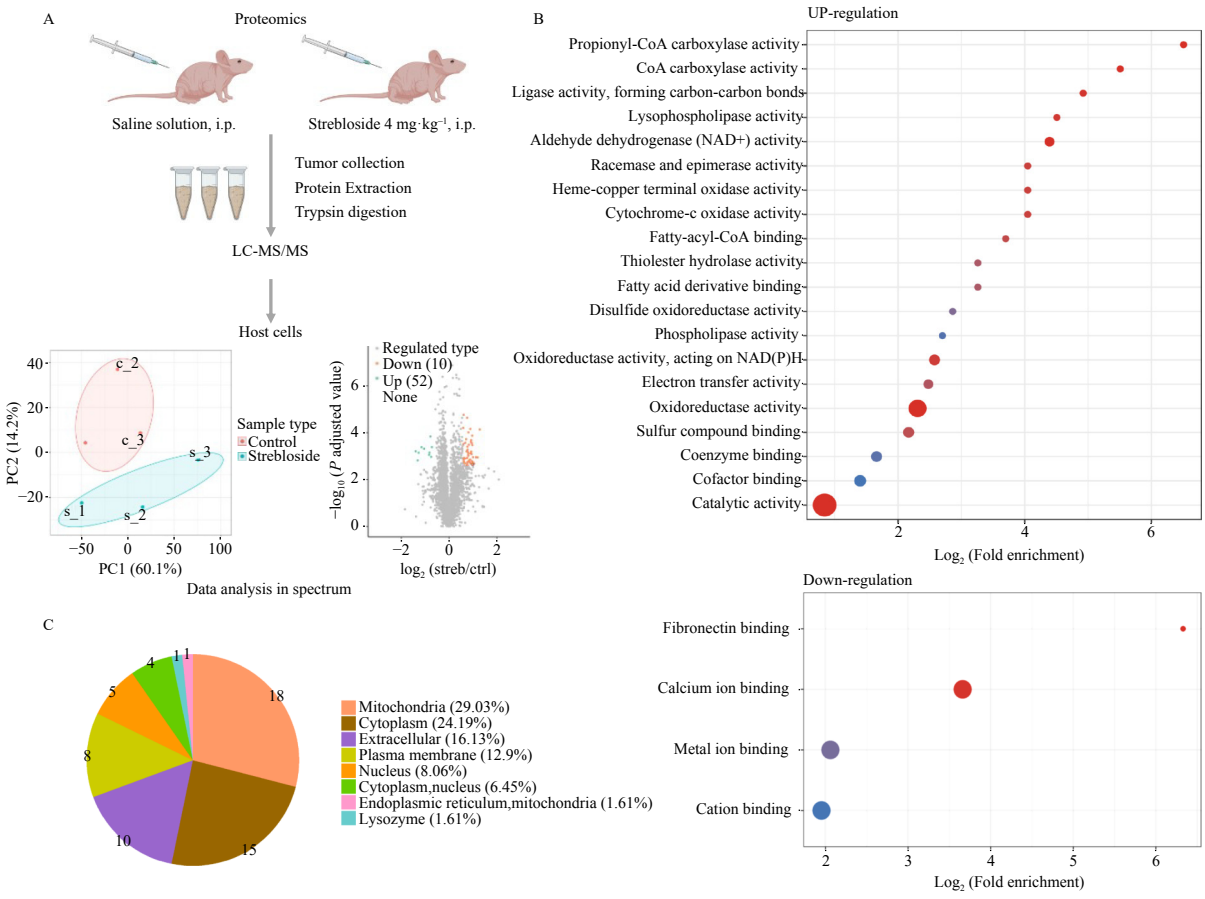

Fig. 3 Proteomics analysis of subcutaneously transplanted tumor in nude mice (A) NHL tumors with no or (+)-strebloside treated were harvested and carried out proteomics analysis flow diagram. (B) Double-tailed Fisher was used to accurately test the enrichment degree of differential proteins on all identified proteins ($P < 0.05$), and molecular functional enrichment analysis of differential proteins was performed based on GO. (C) WolF Psort software was used to locate differential proteins.

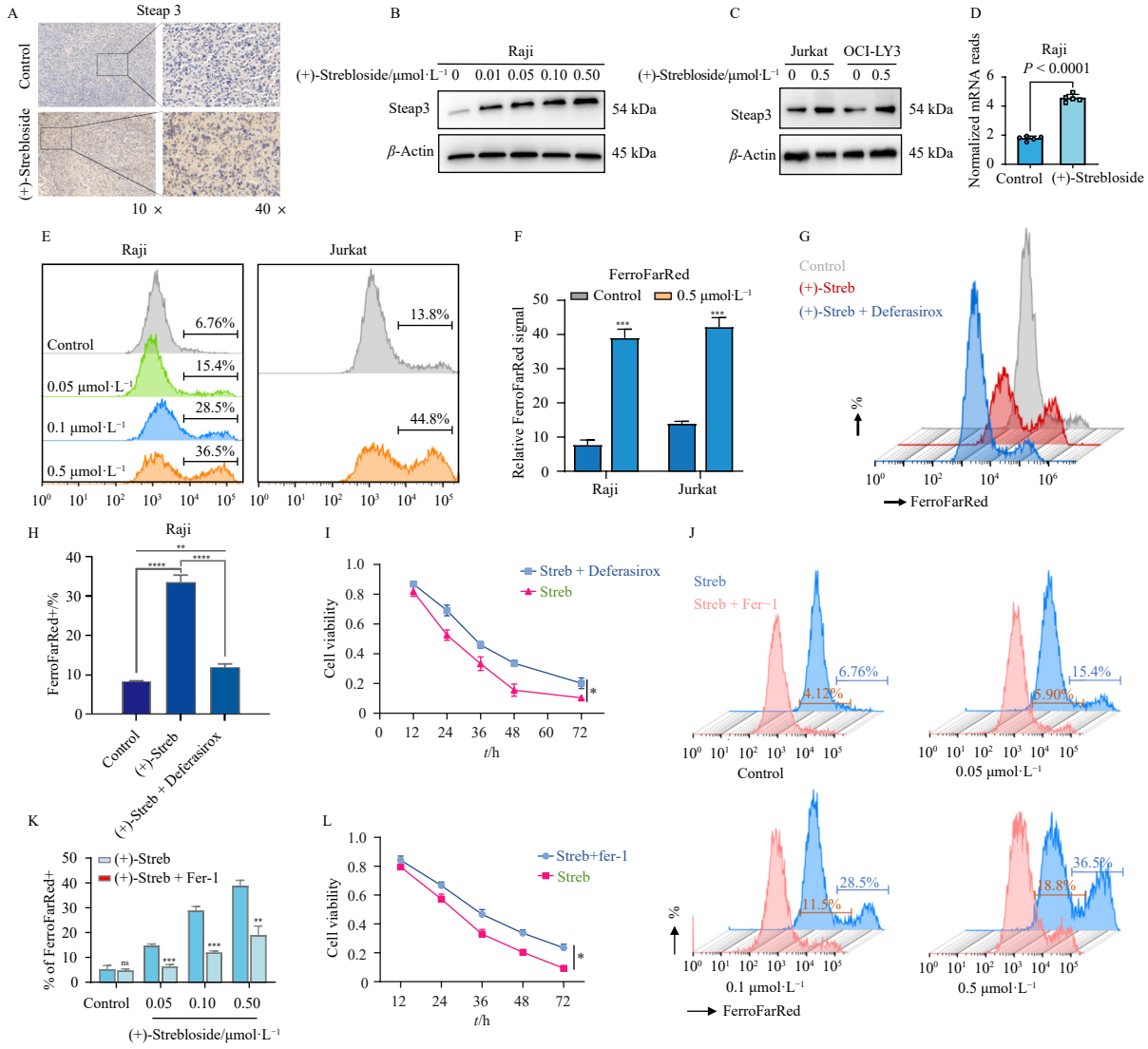

Fig. 4 (+)-Strebloside mediates STEAP3 overexpression and intracellular ferrous ion enrichment in NHL. (A) STEAP3 protein expression in nude mice subcutaneous transplant tumor tissues. Following treatment with different concentrations of (+)-strebloside. (B–C) STEAP3 protein expression levels in NHL cells. (D) STEAP3 nucleic acid expression levels in NHL cells with (+)-strebloside (0.5 μmol·L^{-1}) treatment (n = 5); (E, F) The change of intracellular ferrous ion concentration after (+)-strebloside treatment in NHL cells (n = 3). (G–I) Intracellular ferrous ion content under the co-treatment with chelator of iron ions, deferasirox (5 μmol·L^{-1}) and (+)-strebloside (0.1 μmol·L^{-1}) for 24 h. and the cell viability under the co-treatment with chelator of iron ions, deferasirox (5 μmol·L^{-1}) and (+)-strebloside (0.1 μmol·L^{-1}) for 12–72 h (n = 3). (J–L) Intracellular ferrous ion content of NHL under the co-treatment with ferroptosis inhibitor, Ferrostatin-1 (0.5 μmol·L^{-1}), and (+)-strebloside (0.05, 0.1, 0.5 μmol·L^{-1}) for 24 h, and the cell viability under the co-treatment with ferroptosis inhibitor, Ferrostatin-1 (0.5 μmol·L^{-1}), and (+)-strebloside (0.1 μmol·L^{-1}) for 12–72 h (n = 3). Results are expressed as mean ± SD. $^{*}P < 0.05$; $^{**}P < 0.01$; $^{***}P < 0.001$.

lates within the cell, generating an unstable iron pool. Free ferrous ions initiate the Fenton reaction, resulting in substantial ROS production and lipid peroxidation, ultimately leading to cellular dysfunction and death.

3.6. (+)-Strebloside significantly triggers ferroptosis in NHL cells

Analysis included assessment of intracellular ROS, lipid peroxidation, and Glutathione peroxidase 4 (GPX4) levels. GPX4, the only intracellular glutathione peroxidase capable of reducing liposomal peroxides, functions as a critical ferroptosis marker. As shown in Fig. 5A, flow cytometry analysis revealed significantly elevated ROS levels in (+)-strebloside-treated Raji cells compared to controls, demonstrating that (+)-strebloside treatment increased ROS production at all concentrations. Intracellular lipid peroxide accumulation was detected in Raji cells following BODIPY-C11 lipid peroxide probe labeling (Fig. 5B). Additionally, GPX4 expression levels decreased in a dose-dependent manner (Fig. 5C).

Analysis revealed that (+)-strebloside significantly affects mitochondrial function in Raji cells. The findings demonstrated that (+)-strebloside reduced mitochondrial transmembrane potential (Fig. 5D), decreased ATP production levels (Fig. 5E), and triggered cytochrome c release (Fig. 5F). These results indicate that mitochondrial functional impairment contributes to the iron metabolism-dependent pathway of (+)-strebloside-induced ferroptosis in NHL.

3.7. Inhibition of STEAP3 antagonizes (+)-strebloside-induced glutathione redox imbalance and ferroptosis in NHL cells

To elucidate the essential functions of STEAP3, Raji cells were transfected with siRNA to suppress STEAP3 expression. STEAP3-si2, which demonstrated the highest inhibition efficiency, was selected for subsequent analysis (Fig. 5G). The results revealed that STEAP3 knockdown significantly reversed the reduction in GPX4 expression (Fig. 5H). Moreover, the decreased cell viability was restored following STEAP3 knockdown (Fig. 5I). In summary, these results suggest that (+)-strebloside can induce ferroptosis through STEAP3 in NHL. Similar outcomes were

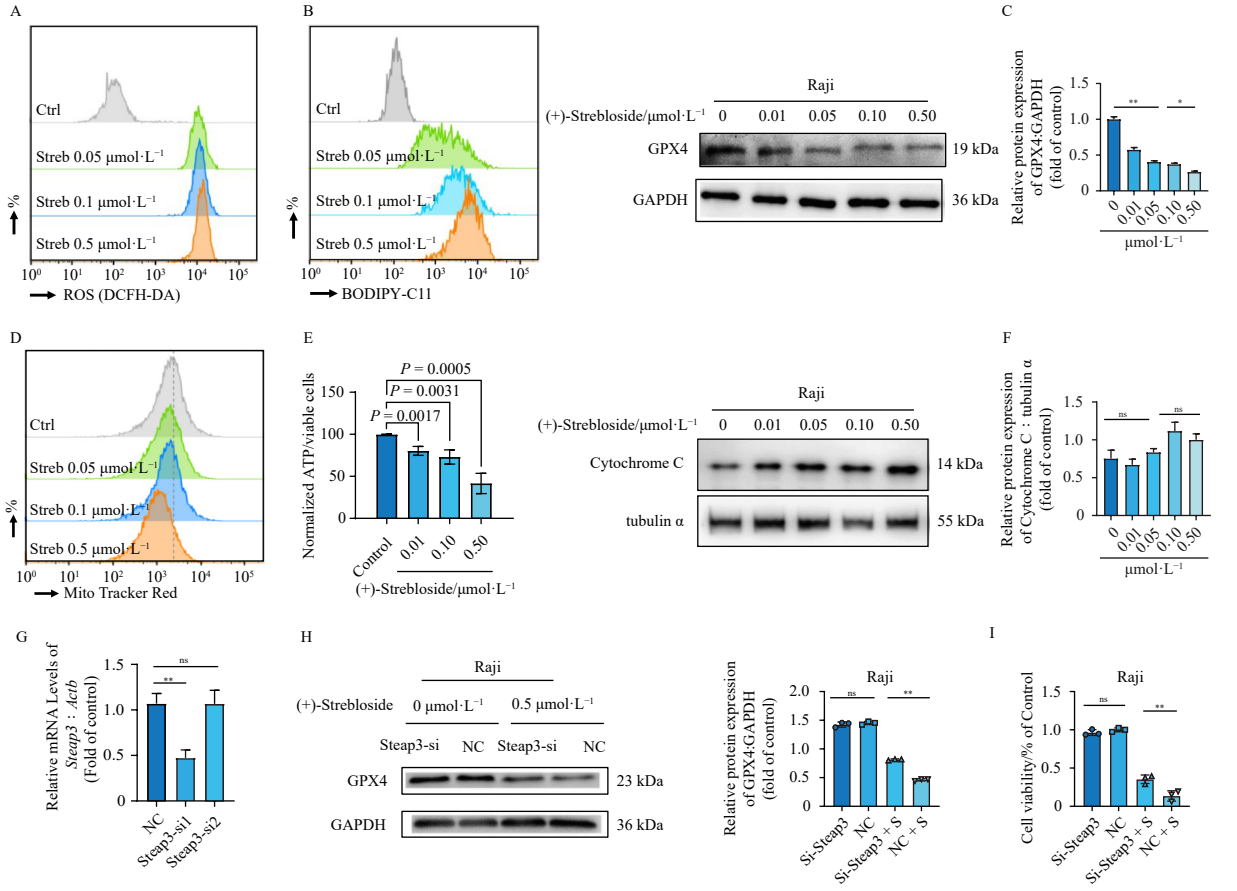

Fig. 5 (+)-Strebloside mediates ferroptosis activation and STEAP3 inhibition antagonized (+)-strebloside-induced ferroptosis in NHL cells. Following treatment with different concentrations of (+)-strebloside, (A) Intracellular ROS levels; (B) Intracellular lipid peroxidation levels; (C) Representative immunoblot of GPX4 (n = 3); (D) Cellular mitochondrial membrane potential levels; (E) Intracellular ATP production level (n = 3); (F) Intracellular cytochrome C release levels (n = 3). (G) The inhibition efficiency of STEAP3-siRNA in NHL cells after transfection with siRNA, NC (negative control) (n = 3); (H) Representative immunoblot and quantification of GPX4 in NHL cells transfected with NC or STEAP3-siRNA and treated with or without (+)-strebloside; (I) Cell viability of NHL cells transfected with NC or STEAP3-siRNA and treated with or without (+)-strebloside (n = 3). Results are expressed as mean ± SD. $^{*}P < 0.05$; $^{**}P < 0.01$; $^{***}P < 0.001$; ns, not significant.

observed in Jurkat cells through cell transfection (Fig. S2). The figures are available in the supplementary materials.

3.8. (+)-Strebloside mediates NHL inhibition of proliferation via the MAPK pathway

Previous research has established that ferroptosis characteristics, including excessive intracellular iron and lipid peroxidation accumulation, can modulate MAPK pathway activity [27,28]. The MAPK pathway serves as a critical regulator of cell growth and survival [29]. This pathway participates in multiple downstream signaling cascades activated by CG compound-mediated NKA inhibition [30]. The present study's proteomic enrichment of differentially expressed proteins associated with metal ion blockage and ion balance disruptions suggests that (+)-strebloside may function as a natural NKA ligand in the MAPK pathway, potentially contributing to tumor growth inhibition.

Further investigation examined the intracellular signaling mechanisms underlying (+)-strebloside's inhibitory effect on NHL proliferation. Western blot analysis revealed that (+)-strebloside treatment increased extracellular signal-regulated kinase (ERK) activity, evidenced by enhanced ERK1/2 phosphorylation [31,32], while c-Jun N-terminal kinase (JNK) activity remained largely unchanged (Figs. 6A–6E). The ERK-specific inhibitor U0126 demonstrates potential in preventing iron-dependent cell death. Results indicated that ERK inhibition significantly reduced Raji cell viability ($P < 0.01$, Figs. 6F–6H) and G_1/S conversion ($P < 0.05$, Figs. 6I and 6J), without affecting cell cycle progression ($P > 0.05$) (Figs. 6H). These findings demonstrate the MAPK pathway's involvement in (+)-strebloside-mediated NHL proliferation inhibition. Similar results were observed in Jurkat cells (Fig. S3). The figures are available in the supplementary material.

The findings indicate that (+)-strebloside reduces iron ions through the upregulation of STEAP3, leading to an accumulation of ferrous ions that participate in the Fenton reaction. This process generates ROS and lipid peroxide, ultimately triggering ferroptosis. Moreover, (+)-strebloside induced cell death in NHL through activation of the MAPK-ERK pathway. The mechanism is depicted in Fig. 7.

4. Discussion

NPs demonstrate significant advantages in treating malignant tumors. Compared to conventional chemotherapy or radiotherapy, NPs are characterized by their diverse sources, enhanced safety profiles, high bioavailability, and extensive bioactivity [33]. CGs, serving as natural NKA ligands, are routinely employed in clinical practice for treating heart failure and atrial arrhythmias [34]. In 1967, Shiratori initially documented that CGs inhibited the proliferation of malignant Hela-S3 cells [35]. Subsequent studies have demonstrated the application of CGs in various cancers, including breast cancer [36–38], prostate cancer [39–41], melanoma [42], pancreatic cancer [43], lung cancer [44,45], renal adenocarcinoma [38], neuroblastoma [46], leukemia [47–49] and numerous other malignancies, exhibiting anti-proliferative and apoptosis-modulating effects. Several CGs have demonstrated cancer therapeutic potential in phase I and phase II clinical trials [50–53], with established pharmacodynamic and pharmacokinetic data facilitating

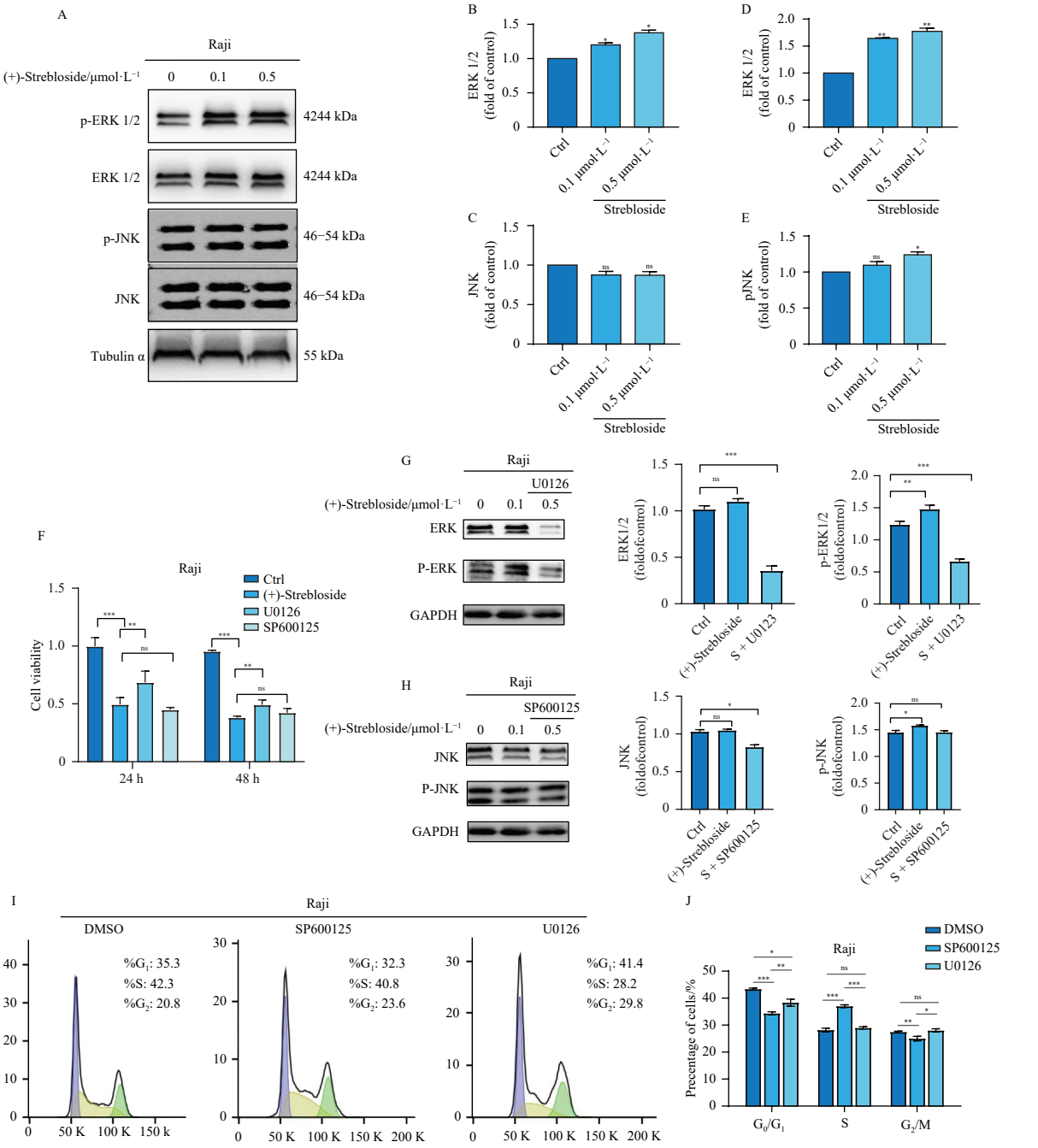

Fig. 6 (+)-Strebloside regulates MAPK-ERK signaling to inhibit NHL cell proliferation. (A) Effect of (+)-strebloside on the expression of key proteins of the MAPK pathway. (B–E) Quantitative maps of MAPK pathway key protein expression (n = 3). (F–H) Effect of ERK1/2 inhibitor(10 μmol·L^{-1}) and JNK(50 μmol·L^{-1}) inhibitor with (+)-strebloside (0.1 μmol·L^{-1}) treatment on Raji cell viability and the expression of proteins of the key MAPK (n = 3). (I, J) Plots of the effect of ERK1/2 inhibitor and JNK inhibitor treatment on the cell cycle of (+)-strebloside-treated Raji cells and quantitative analysis of the cell cycle (n = 3). Results are expressed as mean ± SD. $^{*}P < 0.05$; $^{**}P < 0.01$; $^{***}P < 0.001$; ns, not significant.

further clinical investigation.

This study demonstrates that the CG (+)-strebloside effectively inhibits NHL growth both *in vivo* and *in vitro*. The compound induces apoptosis in NHL cells and arrests their progression at the G_2/M phase *in vivo*. Additionally, (+)-strebloside exhibits minimal systemic toxicity in mice while reducing NHL invasion and metastasis, suggesting potential therapeutic benefits with a favorable safety profile. These observations prompted a detailed investigation of the underlying mechanisms of (+)-strebloside's effects.

STEAP3 functions as an iron transport protein with reductase activity for various metal cations, including iron and copper ions, while also influencing apoptosis and cell cycle progression. Proteomic analysis revealed differential expression of STEAP3 and lipid peroxidation-related proteins. The data suggest that (+)-strebloside utilizes STEAP3 to reduce Fe^{3+} to Fe^{2+}, resulting in intracellular Fe^{2+} accumulation and subsequent participation in the Fenton reaction, generating substantial ROS and inducing ferroptosis. Concentration-dependent STEAP3 expression was confirmed through Western blot, immunohistochemistry, and quantitative PCR analyses following treatment. Further investigation validated additional ferroptosis indicators. Treatment with (+)-strebloside increased intracellular ROS and lipid peroxide levels while decreasing mitochondrial membrane potential, ATP production, GPX4 expression, and promoting cytochrome C release. Moreover, both Deferasirox, an iron-selective chelator, and Fer-1, a ferroptosis inhibitor, attenuated the (+)-strebloside- induced increase in ferrous ions and NHL cell growth

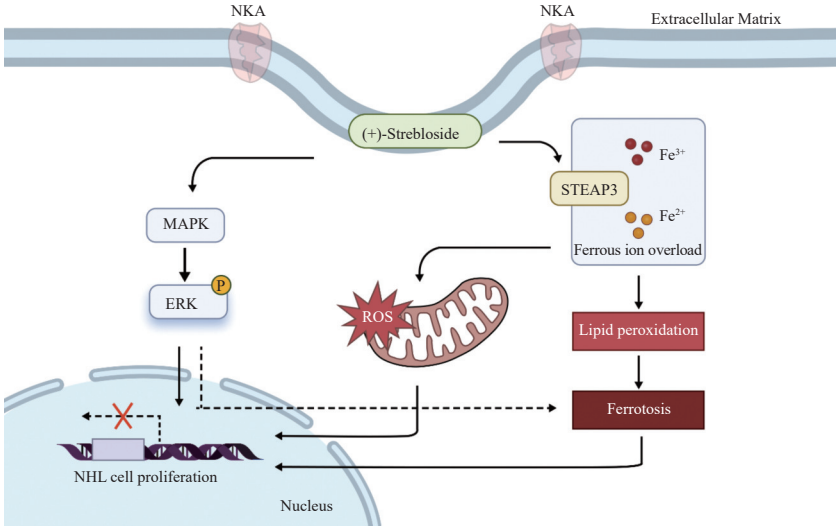

Fig. 7 Schematic diagram of (+)-strebloside inhibiting the NHL progression. Figure created with BioRender.com.

suppression. These findings demonstrate that (+)-strebloside significantly induces ferroptosis in NHL cells.

Further investigation revealed the role of STEAP3 in ferroptosis. The findings demonstrated that STEAP3 knockdown restored both GPX4 expression and cell viability. These results suggest that CG (+)-strebloside mediates ferroptosis through a non-classical iron metabolic pathway in NHL. Additionally, analysis of key proteins in the MAPK signaling pathway revealed increased levels of phosphorylated ERK following (+)-strebloside treatment. This observation indicates the MAPK-ERK pathway's involvement in (+)-strebloside-induced inhibition of NHL cell proliferation. Nevertheless, further investigation is necessary to determine whether (+)-strebloside-induced ferroptosis occurs through the MAPK-ERK pathway and to elucidate NAK's potential role in this mechanism.

5. Conclusion

In conclusion, (+)-strebloside triggers ferroptosis via STEAP3in NHL both in vitro and in vivo, and it also inhibits theprolifera-tion of NHL cells through the MAPK pathway. These findingses-tablish a foundation for future research into (+)-streblos-ide'stherapeutic applications and highlight its potential as apromising treatment option for NHL.

Funding

This work was supported by the "Double First-Class" University Project (No. CPU2018GY34).

Declaration of competing interest

The authors declare that they have no conflicts of interest.

References

1 Armitage JO, Gascoyne RD, Lunning MA, et al. Non-Hodgkin lymphoma. *Lancet*. 2017;390(10091):298-310. https://doi.org/10.1016/S0140-6736(16)32407-2.
2 Siegel RL, Miller KD, Jemal A. Cancer statistics, 2016. *CA Cancer J Clin*. 2016;66(1):7-30. https://doi.org/10.3322/caac.21332.
3 Castillo JJ, Winer ES, Stachurski D, et al. Prognostic factors in chemotherapy-treated patients with HIV-associated Plasmablastic lymphoma. *Oncologist*. 2010;15(3):293-299. https://doi.org/10.1634/theoncologist.2009-0304.
4 Feugier P, Van Hoof A, Sebban C, et al. Long-term results of the R-CHOP study in the treatment of elderly patients with diffuse large B-cell lymphoma: a study by the Groupe d'Etude des Lymphomes de l'Adulte. *J Clin Oncol*. 2005;23(18):4117-4126. https://doi.org/10.1200/JCO.2005.09.131.
5 Susanibar-Adaniya S, Barta SK. 2021 Update on diffuse large B cell lymphoma: a review of current data and potential applications on risk stratification and management. *Am J Hematol*. 2021;96(5):617-629. https://doi.org/10.1002/ajh.26151.
6 Wei J, Liu Y, Wang C, et al. The model of cytokine release syndrome in CAR T-cell treatment for B-cell non-Hodgkin lymphoma. *Signal Transduct Target Ther*. 2020;5(1):134. https://doi.org/10.1038/s41392-020-00256-x.
7 Falchi L, Vardhana SA, Salles GA. Bispecific antibodies for the treatment of B-cell lymphoma: promises, unknowns, and opportunities. *Blood*. 2023;141(5):467-480. https://doi.org/10.1182/blood.2021011994.
8 Harker-Murray PD, Pommert L, Barth MJ. Novel therapies potentially available for pediatric B-cell non-Hodgkin lymphoma. *J Natl Compr Canc Netw*. 2020;18(8):1125-1134. https://doi.org/10.6004/jnccn.2020.7608.
9 Witzig TE, Nowakowski GS, Habermann TM, et al. A comprehensive review of lenalidomide therapy for B-cell non-Hodgkin lymphoma. *Ann Oncol*. 2015;26(8):1667-1677. https://doi.org/10.1093/annonc/mdv102.
10 Maffei R, Fiorcari S, Martinelli S, et al. Targeting neoplastic B cells and harnessing microenvironment: the "double face" of ibrutinib and idelalisib. *J Hematol Oncol*. 2015;8:60. https://doi.org/10.1186/s13045-015-0157-x.
11 Oyama T, Yamamoto K, Asano N, et al. Age-related EBV-associated B-cell lymphoproliferative disorders constitute a distinct clinicopathologic group: a study of 96 patients. *Clin Cancer Res*. 2007;13(17):5124-5132. https://doi.org/10.1158/1078-0432.CCR-06-2823.
12 Morales D, Beltran B, De Mendoza FH, et al. Epstein-Barr virus as a prognostic factor in *de novo* nodal diffuse large B-cell lymphoma. *Leuk Lymphoma*. 2010;51(1):66-72. https://doi.org/10.3109/10428190903308015.
13 Park S, Lee J, Ko YH, et al. The impact of Epstein-Barr virus status on clinical outcome in diffuse large B-cell lymphoma. *Blood*. 2007;110(3):972-978. https://doi.org/10.1182/blood-2007-01-067769.
14 Schatzmann HJ, Räss B. Inhibition of the active Na-K-transport and Na-K-activated membrane ATP-ase of erythrocyte stroma by ouabain. *Helv Physiol Pharmacol Acta*. 1965;65(1):C47-49.
15 Bai Y, Zhu W, Xu Y, et al. Characterization, quantitation, similarity evaluation and combination with Na^+, K^+-ATPase of cardiac glycosides from *Streblus asper*. *Bioorg Chem*. 2019;87:265-275. https://doi.org/10.1016/j.bioorg.2019.03.049.
16 Cai J, Zhang BD, Li YQ, et al. Cardiac glycosides from the roots of *Streblus asper* Lour. with activity against Epstein-Barr virus lytic replication. *Bioorg Chem*. 2022;127:106004. https://doi.org/10.1016/j.bioorg.2022.106004.
17 Chen WL, Ren Y, Ren J, et al. (+)-Strebloside-induced cytotoxicity in ovarian cancer cells is mediated through cardiac glycoside signaling networks. *J Nat Prod*. 2017;80(3):659-669. https://doi.org/10.1021/acs.jnatprod.6b01150.
18 Geng X, Wang F, Tian D, et al. Cardiac glycosides inhibit cancer through Na/K-ATPase-dependent cell death induction. *Biochem Pharmacol*. 2020;182:114226. https://doi.org/10.1016/j.bcp.2020.114226.
19 Murphy MP. Metabolic control of ferroptosis in cancer. *Nat Cell Biol*. 2018;20(10):1104-1105. https://doi.org/10.1038/s41556-018-0209-x.
20 Yuan Y, Xu J, Jiang Q, et al. Ficolin 3 promotes ferroptosis in HCC by downregulating IR/SREBP axis-mediated MUFA synthesis. *J Exp Clin Cancer Res*. 2024;43(1):133. https://doi.org/10.1186/s13046-024-03047-2.
21 Zhang F, Tao Y, Zhang Z, et al. Metalloreductase Steap3 coordinates the regulation of iron homeostasis and inflammatory responses. *Haematologica*. 2012;97(12):1826-1835. https://doi.org/10.3324/haematol.2012.063974.
22 Meng F, Fleming BA, Jia X, et al. Lysosomal iron recycling in mouse macrophages is dependent upon both LcytB and Steap3 reductases. *Blood Adv*. 2022;6(6):1692-1707. https://doi.org/10.1182/bloodadvances.2021005609.
23 Wu L, Tian X, Zuo H, et al. miR-124-3p delivered by exosomes from heme oxygenase-1 modified bone marrow mesenchymal stem cells inhibits ferroptosis to attenuate ischemia-reperfusion injury in steatotic grafts. *J Nanobiotechnol*. 2022;20(1):196. https://doi.org/10.1186/s12951-022-01407-8.
24 Elhassadi E, Hennessy B, Kumar S, et al. Impact of p53 disruption on mantle cell lymphoma (MCL) treatment out-come, multi-centre retrospective study.

Blood. 2021;138(Supplement 1):4514-4514. https://doi.org/10.1182/blood-2021-149653.
25 Chang CC, Cho SF, Chen YW, et al. SUV on dual-phase FDG PET/CT correlates with the Ki-67 proliferation index in patients with newly diagnosed non-Hodgkin lymphoma. *Clin Nucl Med*. 2012;37(8):e189-e195. https://doi.org/10.1097/RLU.0b013e318251e16e.
26 Battaglia AM, Chirillo R, Aversa I, et al. Ferroptosis and cancer: mitochondria meet the "iron maiden" cell death. *Cells*. 2020;9;(6):1505. https://doi.org/10.3390/cells9061505.
27 Yagoda N, von Rechenberg M, Zaganjor E, et al. RAS-RAF-MEK-dependent oxidative cell death involving voltage-dependent anion channels. *Nature*. 2007;447(7146):864-868. https://doi.org/10.1038/nature05859.
28 Chen Y, Fang ZM, Yi X, et al. The interaction between ferroptosis and inflammatory signaling pathways. *Cell Death Dis*. 2023;14(3):205. https://doi.org/10.1038/s41419-023-05716-0.
29 Sun Y, Liu W-Z, Liu T, et al. Signaling pathway of MAPK/ERK in cell proliferation, differentiation, migration, senescence and apoptosis. *J Recept Sig Transd*. 2015;35(6):600-604. https://doi.org/10.3109/10799893.2015.1030412.
30 Wang Z, Zheng M, Li Z, et al. Cardiac glycosides inhibit p53 synthesis by a mechanism relieved by Src or MAPK inhibition. *Cancer Res*. 2009;69(16):6556-6564. https://doi.org/10.1158/0008-5472.CAN-09-0891.
31 Zhu L, Cao P, Yang S, et al. Prolonged exposure to environmental levels of microcystin-LR triggers ferroptosis in brain *via* the activation of Erk/MAPK signaling pathway. *Ecotoxicol Environ Saf*. 2023;267:115651. https://doi.org/10.1016/j.ecoenv.2023.115651.
32 Li J, Gao H, Wang P, et al. Plumbagin induces G_2/M arrest and apoptosis and ferroptosis *via* ROS/p38 MAPK pathway in human osteosarcoma cells. *Alex Eng J*. 2024;103:222-236. https://doi.org/10.1016/j.aej.2024.06.015.
33 Yang Y, Liu Q, Shi X, et al. Advances in plant-derived natural products for antitumor immunotherapy. *Arch Pharm Res*. 2021;44(11):987-1011. https://doi.org/10.1007/s12272-021-01355-1.
34 Rahimtoola SH, Tak T. The use of digitalis in heart failure. *Curr Prob Cardiol*. 1996;21(12):781-853. https://doi.org/10.1016/S0146-2806(96)80001-6.
35 Shiratori O. Growth inhibitory effect of cardiac glycosides and aglycones on neoplastic cells: *in vitro* and *in vivo* studies. *Gan*. 1967;58(6):521-528. https://doi.org/10.20772/CANCERSCI1959.58.6_521.
36 Kometiani P, Liu L, Askari A. Digitalis-induced signaling by Na^+/K^+-ATPase in human breast cancer cells. *Mol Pharmacol*. 2005;67(3):929-936. https://doi.org/10.1124/mol.104.007302.
37 Bielawski K, Winnicka K, Bielawska A. Inhibition of DNA topoisomerases I and II, and growth inhibition of breast cancer MCF-7 cells by ouabain, digoxin and proscillaridin A. *Biol Pharm Bull*. 2006;29(7):1493-1497. https://doi.org/10.1016/S0006-2952(03)00281-8.
38 López-Lázaro M, Pastor N, Azrak SS, et al. Digitoxin inhibits the growth of cancer cell lines at concentrations commonly found in cardiac patients. *J Nat Prod*. 2005;68(11):1642-1645. https://doi.org/10.1021/np050226l.
39 McConkey DJ, Lin Y, Nutt LK, et al. Cardiac glycosides stimulate Ca^{2+} increases and apoptosis in androgen-independent, metastatic human prostate adenocarcinoma cells. *Cancer Res*. 2000;60(14):3807-3812. https://doi.org/10.1016/S0165-4608(00)00214-4.
40 Huang YT, Chueh SC, Teng CM, et al. Investigation of ouabain-induced anticancer effect in human androgen-independent prostate cancer PC-3 cells. *Biocheml Pharmacol*. 2004;67(4):727-733. https://doi.org/10.1016/j.bcp.2003.10.013.
41 Yeh JY, Huang WJ, Kan SF, et al. Effects of bufalin and cinobufagin on the proliferation of androgen dependent and independent prostate cancer cells. *The Prostate*. 2002;54(2):112-124. https://doi.org/10.1002/pros.10172.
42 Newman RA, Yang P, Hittelman WN, et al. Oleandrin-mediated oxidative stress in human melanoma cells. *J Exp Therapeut Oncol*. 2006;5(3):167-181.
43 Newman RA, Kondo Y, Yokoyama T, et al. Autophagic cell death of human pancreatic tumor cells mediated by oleandrin, a lipid-soluble cardiac glycoside. *Integr Cancer Ther*. 2007;6(4):354-364. https://doi.org/10.1177/1534735407309623.
44 Mijatovic T, Op De Beeck A, Van Quaquebeke E, et al. The cardenolide UNBS1450 is able to deactivate nuclear factor κB–mediated cytoprotective effects in human non–small cell lung cancer cells. *Mol Cancer Therapeut*. 2006;5(2):391-399. https://doi.org/10.1158/1535-7163.MCT-05-0367.
45 Frese S, Frese-Schaper M, Andres AC, et al. Cardiac glycosides initiate Apo2L/TRAIL-induced apoptosis in non-small cell lung cancer cells by up-regulation of death receptors 4 and 5. *Cancer Res*. 2006;66(11):5867-5874. https://doi.org/10.1158/0008-5472.CAN-05-3544.
46 Kulikov A, Eva A, Kirch U, et al. Ouabain activates signaling pathways associated with cell death in human neuroblastoma. *BBA-Biomembranes*. 2007;1768(7):1691-1702. https://doi.org/10.1016/j.bbamem.2007.04.012.
47 Masuda Y, Kawazoe N, Nakajo S, et al. Bufalin induces apoptosis and influences the expression of apoptosis-related genes in human leukemia cells. *Leukemia Res*. 1995;19(8):549-556. https://doi.org/10.1016/0145-2126(95)00031-I.
48 Daniel D, Susal C, Kopp B, et al. Apoptosis-mediated selective killing of malignant cells by cardiac steroids: maintenance of cytotoxicity and loss of cardiac activity of chemically modified derivatives. *Int Immunopharmacol*. 2003;3(13-14):1791-1801. https://doi.org/10.1016/j.intimp.2003.08.004.
49 Watabe M, Kawazoe N, Masuda Y, et al. Bcl-2 protein inhibits bufalin-induced apoptosis through inhibition of mitogen-activated protein kinase activation in human leukemia U937 cells. *Cancer Res*. 1997;57(15):3097-3100.
50 Platz EA, Yegnasubramanian S, Liu JO, et al. A novel two-stage, transdisciplinary study identifies digoxin as a possible drug for prostate cancer treatment. *Cancer Discov*. 2011;1(1):68-77. https://doi.org/10.1158/2159-8274.CD-10-0020.
51 Galluzzi L, Senovilla L, Zitvogel L, et al. The secret ally: immunostimulation by anticancer drugs. *Nat Rev Drug Discov*. 2012;11(3):215-233. https://doi.org/10.1038/nrd3626.
52 Roth MT, Cardin DB, Borazanci EH, et al. A phase II, single-arm, open-label, bayesian adaptive efficacy and safety study of PBI-05204 in patients with stage IV metastatic pancreatic adenocarcinoma. *Oncologist*. 2020;25(10):e1446-e1450. https://doi.org/10.1634/theoncologist.2020-0440.
53 Hong DS, Henary H, Falchook GS, et al. First-in-human study of pbi-05204, an oleander-derived inhibitor of akt, fgf-2, nf-kappaBeta and p70s6k, in patients with advanced solid tumors. *Invest New Drugs*. 2014;32(6):1204-1212. https://doi.org/10.1007/s10637-014-0127-0.